

Realtime Multi-Person 2D Pose Estimation using Part Affinity Fields *

Zhe Cao Tomas Simon Shih-En Wei Yaser Sheikh
 The Robotics Institute, Carnegie Mellon University
 {zhecao, shihenw}@cmu.edu {tsimon, yaser}@cs.cmu.edu

Abstract

We present a realtime approach for multi-person 2D pose estimation that predicts vector fields, which we refer to as Part Affinity Fields (PAFs), that directly expose the association between anatomical parts in an image. The architecture is designed to jointly learn part locations and their association, via two branches of the same sequential prediction process. The sequential prediction enables the part confidence maps and the association fields to encode global context, while allowing an efficient bottom-up parsing step that maintains tractable runtime complexity. Our method has set the state-of-the-art performance on the inaugural MSCOCO 2016 keypoints challenge, and significantly exceeds the previous state-of-the-art result on the MPII Multi-Person benchmark, both in performance and efficiency.

1. Introduction

Human 2D pose estimation—the problem of localizing anatomical landmarks or “parts”—has largely focused on finding parts of *individuals* [23, 38, 6]. Inferring the pose of multiple people in images, especially socially engaged individuals, presents a unique set of challenges. First, each image may contain an unknown number of people that may occur at any position or scale. Second, interactions between people induce complex spatial interference, due to contact, occlusion, and limb articulations, making association of parts difficult. Third, runtime complexity is prone to grow with the number of people in the image, making realtime performance a challenge.

A common approach [28, 11, 33, 16] is to divide and conquer the problem by employing a person detector and performing single-person pose estimation for each detection. These top-down approaches directly leverage existing techniques for single-person pose estimation, but suffer from early commitment: if the person detector fails—as it is prone to do when people are in close proximity—there is no recourse to recovery. Furthermore, the runtime of these

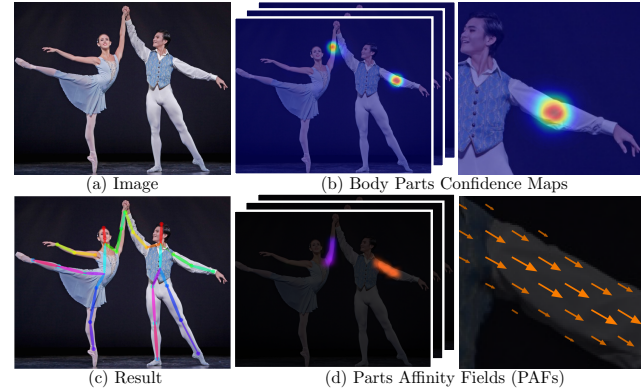
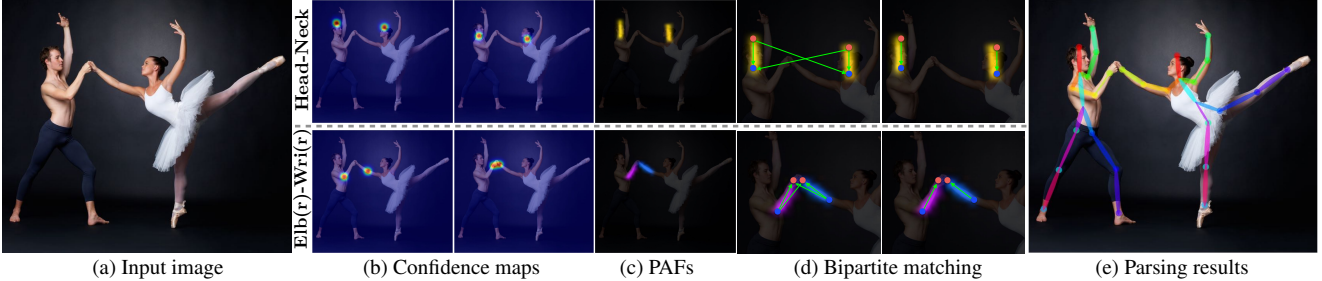


Figure 1. Representations for body parts detection and association. (a) Original Image. (b) The part confidence map. There are peaks at the part locations. (c) Pose estimation result. (d) Part affinity fields. Color encodes the orientation of human limbs, where the one connecting left shoulder and left elbow is shown. The size of the arrow represents magnitude of predicted vectors.

top-down approaches is proportional to the number of people: for each detection, a single-person pose estimator is run, and the more people there are, the greater the computational cost. In contrast, bottom up approaches are attractive as they offer robustness to early commitment and have the potential to decouple runtime complexity from the number of people detected in the image. Yet, bottom-up approaches do not benefit directly from global information, which is critical in utilizing contextual cues from other body parts and other people.

In this paper, we present a method for multi-person pose estimation that approaches the problem in a bottom-up manner to maintain realtime performance and robustness to early commitment, but utilizes global contextual information in the detection of parts and their association. In particular, we present Part Affinity Fields (PAFs), a set of 2D vector fields, each of which encode the location and orientation of a particular limb at each position in the image domain. These fields are learned and predicted jointly with confidence maps for parts, within a sequential prediction framework that allows global context to inform the estimates of parts and their associations. As both the part confidence maps and the part affinity fields are 2D spatial

*Video result: <http://posefs1.perception.cs.cmu.edu/Users/ZheCao/humanpose.mp4>



(a) Input image

Head-Neck

Elb(r)-Wri(r)

(b) Confidence maps

(c) PAFs

(d) Bipartite matching

(e) Parsing results

Figure 2. Overall pipeline. Our method takes the entire image as the input for a two-branch CNN to jointly predict confidence maps for body part detection, shown in the (b), and part affinity fields for parts association, shown in the (c). The parsing step performs a set of bipartite matching to associate body parts candidates (d) and finally assemble them into full body poses for all people in the image (e).

grids, they can represent unstructured, multimodal uncertainty that arises due to occlusion and contact; furthermore, they are amenable to convolutional analysis. As the confidence maps and affinity fields encode global context in their prediction, they allow an efficient algorithm that uses greedy association over a minimum spanning tree without significant loss in the quality of pose estimates. We report results on the inaugural MSCOCO 2016 challenge where our approach sets the state-of-the-art, and in the MPII multi-person benchmark, where we significantly exceed the previous state-of-the-art result. Finally, we will release the code publicly for full reproducibility, presenting the first realtime system for multi-person 2D pose detection.

2. Related Work

The traditional approach to articulated human pose estimation is to perform inference over a combination of local observations on body parts and the spatial dependencies between them. The spatial model for articulated pose is either based on tree-structured graphical models [10, 30, 4, 3, 26, 40, 17], which parametrically encode the spatial relationship between adjacent parts following a kinematic chain, or non-tree models [37, 31, 20, 18, 8] that augment the tree structure with additional edges to capture occlusion, symmetry, and long-range relationships. To obtain reliable local observations of body parts, Convolutional Neural Networks (CNNs) have been widely used, and have significantly boosted the accuracy on body pose estimation [23, 38, 24, 34, 35, 7, 36, 6]. Tompson et al. [35] used a deep architecture with a graphical model whose parameters are learned jointly with the network. Pfister et al. [25] further used CNNs to implicitly capture global spatial dependencies by designing networks with large receptive fields. The convolutional pose machines architecture proposed by Wei et al. [38] used a multi-stage architecture based on a sequential prediction framework [29]; iteratively incorporating global context to refine part confidence maps and preserving multimodal uncertainty from previous iterations. Intermediate supervisions are enforced at the end of each stage to address the problem of vanish-

ing gradients [14, 12, 5] during training. Newell et al. [23] also showed intermediate supervisions are beneficial even in ResNet [13] based architectures. However, all of these methods assume a single person settings where the location and scale of the interested person are given.

For multi-person pose estimation, most approaches [28, 11, 33, 16] have used a top-down strategy that first detects people and then on each detected region have estimated the pose of each person independently. Although this strategy makes the techniques developed for single person case directly applicable, it not only suffers from early commitment on person detection, but also fails to capture the spatial dependencies across different people that require global inference. Some approaches have started to consider inter-person dependencies. Eichner et al. [9] extended pictorial structures to take a set of interacting people and depth ordering into account, but still required a person detector to initialize detection hypotheses. Pishchulin et al. [27] proposed a bottom-up approach that jointly labels part detection candidates and associated them to individual people, with pairwise scores regressed from spatial offsets of detected parts. This approach does not rely on person detections, however, solving the proposed integer linear programming over the fully connected graph is an NP-hard problem and thus the average processing time for a single image is on the order of hours. Insafutdinov et al. [15] built on [27] with a stronger part detectors based on ResNet [13] and image-dependent pairwise scores, and vastly improved the runtime with an incremental optimization approach, but the method still takes several minutes per image, with a limit of at most 150 part proposals. The pairwise representations used in [15], which are offset vectors between every pair of body parts, are difficult to regress precisely and thus a separate logistic regression is required to convert the pairwise features into a probability score.

In this work, we achieve realtime performance for multi-person pose estimation. We present a novel representation PAFs which consist a set of flow fields to encode unstructured pairwise relationships between body parts of a variable number of people. As with confidence maps of body parts, this representation also preserves multi-modal uncer-

tainty and is suitable for analysis using CNNs. We build a two-branch network upon CPMs [38] to iteratively refine both confidence maps and PAFs with global image and spatial contexts. In contrast to [27, 15], we can efficiently obtain pairwise scores from PAFs without an additional training step. Moreover, since these scores are already determined by considering global context (via the sequential prediction framework), we show that a greedy algorithm to assemble body parts in a tree-structured model is sufficient to produce high quality multi-person pose estimation, without requiring a computationally expensive optimization on fully connected graphs.

3. Method

Body part detection and part association are the two principal tasks in our bottom-up approach for multi-person pose estimation. Figure 2 illustrates the overall pipeline of our method. In this section, we first introduce the learning objectives for the two tasks. Then we describe how the predicted representations are efficiently used for obtaining multi-person poses. Finally, we describe our architectural design for predicting these representations.

3.1. Confidence Maps for Part Detection

For body part detection, we use the confidence map representation which models the part locations as Gaussian peaks in the map as shown in Figure 2(b). Let $\mathbf{x}_{j,k} \in \mathbb{R}^2$ be the ground-truth position of body part j for person k in the image, the value of location $\mathbf{p} \in \mathbb{R}^2$ in the confidence map $\mathbf{S}_{j,k}$ for person k is defined as,

$$\mathbf{S}_{j,k}^*(\mathbf{p}) = \exp\left(-\frac{\|\mathbf{p} - \mathbf{x}_{j,k}\|_2^2}{\sigma}\right), \quad (1)$$

where σ is empirically chosen, $\mathbf{S}_j^* \in \mathbb{R}^{w \times h}$, w and h are dimensions of the image. The ideal confidence map to be predicted by the network is an aggregation of peaks of all people in a single map via a max operator,

$$\mathbf{S}_j^*(\mathbf{p}) = \max_k \mathbf{S}_{j,k}^*(\mathbf{p}), \quad (2)$$

We take the maximum of the confidence maps instead of average so that the precision of close-by peaks remain distinct, as illustrated in Figure 3(a). At test time, we obtain body part candidates by performing non-maximum suppression on the predicted confidence maps.

3.2. Part Affinity Fields for Part Association

Given a set of detected body parts, how do we assemble them to form the full-body poses of an unknown number of people? We need a measurement of the confidence for each pair of two body part detections that they are associated, i.e., from the same person. Inspired by Yang et

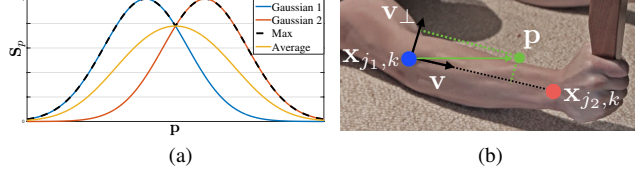


Figure 3. (a) The maximum and average of two Gaussian peaks close-by. (b) Criterion for checking if position \mathbf{p} is in the limb area.

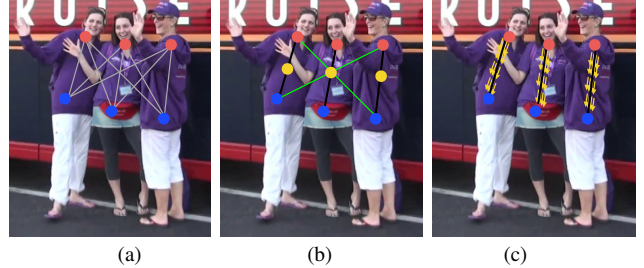


Figure 4. Part association via intermediate representations. (a) The body part detection candidates (red and blue dots) for two body part types and all connection candidates (grey lines). (b) The connection results using the midpoint (yellow dots) representation: correct connections (black lines) and incorrect connections (green lines) that also satisfy the incidence constraint. (c) The results using PAFs (yellow arrows).

al. [41] which augments the tree model with additional parts on each limb, one possible way to obtain this measurement is to predict confidence maps for n interpolated midpoints along the line segment connecting two body parts. We denote the confidence map for the i th midpoint as \mathbf{S}_{c_i} , where $i \in \{1 \dots n\}$, $c \in \{1 \dots C\}$, C is the number of limb types¹. We further define \mathbf{S}_c as maximum of confidence maps of the n midpoints confidence maps of limb c . Consider a limb type c (e.g., left forearm) that joins body parts of type j_1 and $j_2 \in \{1 \dots J\}$ (e.g., left elbow and left wrist), where J is the number of body parts. We can measure the association score between a part candidate of j_1 at position \mathbf{d}_{j_1} and a part candidate of j_2 at position \mathbf{d}_{j_2} by integrating confidence along the limb:

$$E = \int_{u=0}^{u=1} \mathbf{S}_c(\mathbf{p}(u)) du, \quad (3)$$

where $\mathbf{p}(u)$ interpolates the position of the two body parts \mathbf{d}_{j_1} and \mathbf{d}_{j_2} ,

$$\mathbf{p}(u) = (1 - u)\mathbf{d}_{j_1} + u\mathbf{d}_{j_2}. \quad (4)$$

However, the midpoint representation has spatial ambiguity due to possible overlapping midpoints. Figure 4(b) shows such an ambiguity for the case of $n = 1$, i.e., one midpoint, but even for higher values of n , ambiguities can arise in configurations that commonly occur in multi-person images. A

¹We refer to part pairs as limbs for clarity, despite the fact that some pairs are not human limbs (e.g., the face).

key limitation of such intermediate parts is that they encode only the location information and eschew orientation information of the limb.

To solve this, we present a novel feature representation we call a *part affinity field* that preserves both location and orientation information required to perform body part association. The part affinity is a vector field, as shown in Figure 1(d): for each pixel in the area belonging to a particular limb type, a 2D vector encodes the direction that points from one part to the other. Each type of limb has an associated affinity field joining its two associated body parts. If we consider a single limb, let $\mathbf{x}_{j_1, k}$ and $\mathbf{x}_{j_2, k}$ be the position of body parts j_1 and j_2 from the limb class c for a person k on the image. $l_{c, k} = \|\mathbf{x}_{j_2, k} - \mathbf{x}_{j_1, k}\|_2$ is the length of the limb, and $\mathbf{v} = l_{c, k}^{-1}(\mathbf{x}_{j_2, k} - \mathbf{x}_{j_1, k})$ is the unit vector in the direction of the limb. We define the ideal part affinity vector field, $\mathbf{L}_{c, k}^*$, at an image point \mathbf{p} as

$$\mathbf{L}_{c, k}^*(\mathbf{p}) = \begin{cases} \mathbf{v} & \text{if } \mathbf{p} \text{ on limb } c, k \\ \mathbf{0} & \text{otherwise,} \end{cases} \quad (5)$$

where the set of points on the limb is defined as those within a distance threshold of the line segment, i.e.,

$$0 \leq \mathbf{v} \cdot (\mathbf{p} - \mathbf{x}_{j_1, k}) \leq l_{c, k} \text{ and } |\mathbf{v}_\perp \cdot (\mathbf{p} - \mathbf{x}_{j_1, k})| \leq \sigma_l,$$

with σ_l a distance in pixels defining the limb width, and \mathbf{v}_\perp a vector perpendicular to \mathbf{v} , as shown in Figure 3(b). The ideal part affinity field to be predicted by the network combines the limbs of type c of all people into a single map,

$$\mathbf{L}_c^*(\mathbf{p}) = \frac{1}{n_p} \sum_k \mathbf{L}_{c, k}^*(\mathbf{p}), \quad (6)$$

where $\mathbf{L}_c^* \in \mathbb{R}^{w \times h \times 2}$, n_p is the number of non-zero vectors at point \mathbf{p} across all k people (i.e., the average at pixels where different people's limbs overlap).

During testing, we obtain the confidence score of each limb candidate (i.e., each pair of possible connections between detected body parts) by measuring the alignment of the predicted PAF with the candidate limb that would be formed by connecting the detected body parts. We measure this alignment at points along the line segment that connects the two detected body parts, \mathbf{d}_{j_1} and \mathbf{d}_{j_2} , sampling the predicted part affinity field, \mathbf{L}_c , along that segment:

$$E = \int_{u=0}^{u=1} \mathbf{L}_c(\mathbf{p}(u)) \cdot \frac{\mathbf{d}_{j_2} - \mathbf{d}_{j_1}}{\|\mathbf{d}_{j_2} - \mathbf{d}_{j_1}\|_2} du, \quad (7)$$

In practice, we approximate the integral by sampling and summing uniformly-spaced values of u .

3.3. Multi-Person Parsing using PAFs

The confidence maps and part affinity fields described in the previous section enables us to design a greedy parsing

algorithm based on a tree-structure that produces efficient inference at runtime. Due to the sequential prediction architecture, which utilizes global context for the inference of both the part confidence maps and the affinity fields, the bottom-up algorithm produces high quality parses.

We first obtain a set of body part detection candidates \mathcal{D}_J for multiple people using nonmaxima suppression on each predicted confidence map, where $\mathcal{D}_J = \{\mathbf{d}_j^m : \text{for } j \in \{1 \dots J\}, m \in \{1 \dots N_j\}\}$, with N_j the number of candidates of part type j , and $\mathbf{d}_j^m \in \mathbb{R}^2$ the location of the m -th detection candidate of body part type j . These part detection candidates still need to be associated with other parts from the same person—in other words, we need to find the pairs of part detections that are in fact connected limbs. We define a variable $z_{mnj_1j_2} \in \{0, 1\}$ to indicate whether two detection candidates $\mathbf{d}_{j_1}^m$ and $\mathbf{d}_{j_2}^n$ are connected, and the goal is to find the optimal assignment for the set of all possible connections, $\mathcal{Z} = \{z_{mnj_1j_2} : \text{for } j_1, j_2 \in \{1 \dots J\}, m \in \{1 \dots N_{j_1}\}, n \in \{1 \dots N_{j_2}\}\}$.

Finding these connections reduces to a maximum weight bipartite graph matching problem [39] if we consider a *single* pair of part types j_1 and j_2 (e.g., neck and right hip) for the c th limb. This case is shown in Figure 4(a). In this graph matching problem, nodes of the graph are the body part detection candidates \mathcal{D}_{j_1} and \mathcal{D}_{j_2} , and edges are all possible connections between pairs of detection candidates. Additionally, each edge is weighted by Equation 7—the part affinity aggregate. A matching in a bipartite graph is a subset of the edges chosen in such a way that no two edges share an node. Our goal is to find a matching with maximum weight for the chosen edges. Mathematically,

$$\max E_c = \max_{\mathcal{Z}_c} \sum_{m \in \mathcal{D}_{j_1}} \sum_{n \in \mathcal{D}_{j_2}} E_{mn} \cdot z_{mnj_1j_2}, \quad (8)$$

$$\forall m \in \mathcal{D}_{j_1}, \sum_{n \in \mathcal{D}_{j_2}} z_{mnj_1j_2} \leq 1, \quad (9)$$

$$\forall n \in \mathcal{D}_{j_2}, \sum_{m \in \mathcal{D}_{j_1}} z_{mnj_1j_2} \leq 1, \quad (10)$$

where E_c is the overall weight of the matching from limb type c , \mathcal{Z}_c is the subset of \mathcal{Z} for limb type c , E_{mn} is the part affinity between parts $\mathbf{d}_{j_1}^m$ and $\mathbf{d}_{j_2}^n$. Equations 9 and 10 enforce no two edges share an node, i.e., no two limbs of the same type (e.g., left forearm) share a part. We use the Hungarian algorithm [19] to obtain the maximum matching.

When it comes to finding the full body pose of multiple people, determining \mathcal{Z} is a problem of maximum weight cliques partition in the K -partite graph, as shown in Figure 5(a). A clique in the graph is a subset of nodes within which every two nodes are adjacent. This problem is NP hard [39] and many relaxations exist. In this work, we add two relaxations to the optimization. First, we choose a minimal number of edges to obtain a tree skeleton of human

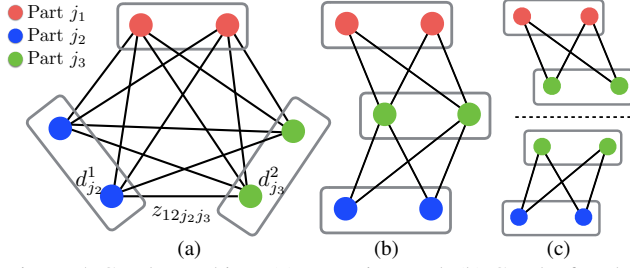


Figure 5. Graph matching. (a) K-partite graph (b) Graph after the tree relaxation (c) A set of bipartite graphs after relaxation

pose rather than using the complete graph, as shown in Figure 5(b). Second, we further decompose the cliques partition problem into a set of bipartite matching subproblems and decide the matching in adjacent tree nodes independently, as shown in Figure 5(c). We argue that minimal greedy can still maintain some properties of global inference over multiple people. The reason is that the relationship between adjacent tree nodes is modeled explicitly by PAFs, but internally, the relationship between nonadjacent tree nodes is implicitly modeled by the CNN. This is because the CNN is trained with a large receptive field, and PAFs from non-adjacent tree nodes also influence the predicted PAF, as will be described in Section 3.4. With these two relaxations, the optimization is decomposed simply as:

$$\max_{\mathcal{Z}} E = \sum_{c=1}^C \max_{\mathcal{Z}_c} E_c. \quad (11)$$

We therefore obtain the correct connection candidates for each human limb class sequentially using Equation 8- 10. With all limb connection candidates, we can assemble these connections which share same part detection candidate into full-body poses of multiple people. It is notable that we directly utilize the PAFs prediction to obtain the weight of the graph edge and avoid the additional step to learn a regressor such as [15]. Our optimization scheme over the tree structure is an order of magnitude faster than the optimization over the fully connected graph [27, 15].

3.4. Joint Learning Part Detection and Association with Sequential Prediction

For learning the representations for body parts detection and parts association, we design an architecture that learns to predict both jointly, because they share common visual clues to infer and are tightly coupled spatially. Several previous approaches train these two tasks separately (e.g., CNNs for parts detection followed by graphical models for association), due to the lack of a representation amenable to joint learning. PAFs for parts association are suitable to be jointly learned with the parts confidence maps for parts detection in one end-to-end trainable CNN. CNNs have been shown to be capable of iteratively refining confidence maps by learning implicit spatial relationship between different

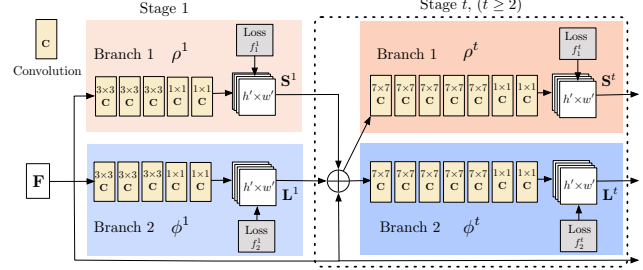


Figure 6. Architectural design of our two-branch multi-stage CNN. Each stage in the first branch is predicting confidence score maps, and each stage in the second branch is predicting PAFs. After each stage, the predictions from the two branches together with the image features \mathbf{F} produced in stage 1, are concatenated for next stage.

body parts in the single person case [38]; we show the that sequential prediction architectures can also iteratively refine PAFs while capturing spatial relationship across different people as well. Figure 7 shows an example.

Our architectural design is shown in Figure 6. The network has multiple stages with intermediate supervision at the end of each stage $t \in \{1 \dots T\}$. In the first stage, the first 10 layers learn image features \mathbf{F} which are used by all subsequent stages. During training, we initialize the 10 layers from the VGG-19 [32]. To jointly predict the two types of representation that share visual features, we split the network into two branches at 5 layers before the losses. The network after the splitting point can be denoted as $\mathbf{S}^1 = \rho^1(\mathbf{F})$ and $\mathbf{L}^1 = \phi^1(\mathbf{F})$, where $\mathbf{S}^1 = (\mathbf{S}_1^1, \mathbf{S}_2^1, \dots, \mathbf{S}_J^1)$ and $\mathbf{L}^1 = (\mathbf{L}_1^1, \mathbf{L}_2^1, \dots, \mathbf{L}_C^1)$, $\rho^t(\cdot)$ and $\phi^t(\cdot)$ are CNNs to be learned in stage t . In every subsequent stages, the predictions from both branch in last stage, as well as image feature \mathbf{F} produced in stage 1, are concatenated first and then branched out again to refine predictions. That is,

$$\mathbf{S}^t = \rho^t(\mathbf{F}, \mathbf{S}^{t-1}, \mathbf{L}^{t-1}), \quad \forall t \geq 2, \quad (12)$$

$$\mathbf{L}^t = \phi^t(\mathbf{F}, \mathbf{S}^{t-1}, \mathbf{L}^{t-1}), \quad \forall t \geq 2. \quad (13)$$

To guide the network to repeatedly predict confidence maps of body parts in the first branch and the PAFs in the second branch, we apply two loss functions at the end of each stage, one at a branch respectively. We simply use an L_2 loss between the predictions and the ideal representations as described for both branches. Here, we weight the loss functions spatially to address a practical issue that some dataset do not completely label all people, with the supplied masks that indicate those areas possibly containing unlabeled people. To be specific, our loss functions at both branches at stage t are:

$$f_1^t = \sum_{j=1}^J \sum_{\mathbf{p} \in \mathbf{I}} \mathbf{W}(\mathbf{p}) \cdot \|\mathbf{S}_j^t(\mathbf{p}) - \mathbf{S}_j^*(\mathbf{p})\|_2^2, \quad (14)$$

$$f_2^t = \sum_{c=1}^C \sum_{\mathbf{p} \in \mathbf{I}} \mathbf{W}(\mathbf{p}) \cdot \|\mathbf{L}_c^t(\mathbf{p}) - \mathbf{L}_c^*(\mathbf{p})\|_2^2, \quad (15)$$

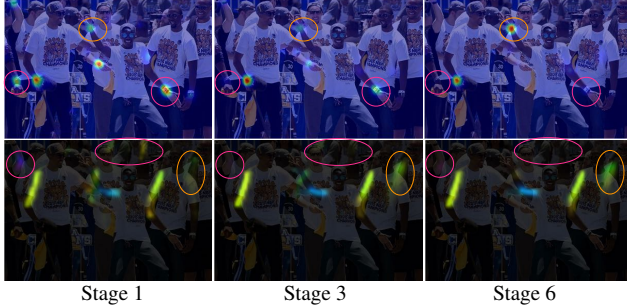


Figure 7. Comparison between the confidence maps of right wrist (the first row) and PAFs (the second row) of right forearm across stages. Although they are often confused by symmetric body parts and limbs in early stage, they are increasingly refined through global inference in later stages, as shown in the highlight area.

where \mathbf{W} is the binary mask, $\mathbf{W}(\mathbf{p}) = 0$ when \mathbf{p} is in the area of persons without annotation. The mask is used to avoid penalizing the true positive predictions during training. The intermediate supervision at each stage addresses the vanishing gradient problem by replenishing the gradient periodically [38]. The overall objective is

$$f = \sum_{t=1}^T (f_1^t + \lambda f_2^t), \quad (16)$$

where λ is a weighting factor that is empirically found to work best when $\lambda = 1$.

4. Results

We evaluate our method on two benchmarks for multi-person pose estimation: (1) the MPII human multi-person dataset [2] and (2) the MSCOCO 2016 keypoints challenge dataset [21]. These two dataset collect images in diverse scenarios of multi-person poses that contain many real-world challenges such as crowding, scale variation, occlusion, and contact. Our approach sets the state-of-the-art on the inaugural MSCOCO 2016 keypoints challenge, and significantly exceeds the previous state-of-the-art result on the MPII multi-person benchmark. We also provide runtime analysis to quantify the efficiency of the system. Figure 10 shows some qualitative results from our algorithm. Videos of our realtime system are in supplementary materials.

4.1. Results on the MPII Multi-Person Dataset

For comparison on the MPII dataset, we use the toolkit provided by the authors [27], which measures mean Average Precision (mAP) of all body parts based on PCKh threshold. Table 1 compares mAP performance between our method and other approaches on the same subset of 288 testing images as in [27], and the entire MPI testing set. Besides these measures, we compare the average processing time per image in seconds. For the 288 images subset,

Method	Hea	Sho	Elb	Wri	Hip	Kne	Ank	mAP	s/image
Subset of 288 images as in [27]									
Deepcut [27]	73.4	71.8	57.9	39.9	56.7	44.0	32.0	54.1	57995
Iqbal et al. [16]	70.0	65.2	56.4	46.1	52.7	47.9	44.5	54.7	10
DeeperCut [15]	87.9	84.0	71.9	63.9	68.8	63.8	58.1	71.2	230
Ours - 6 stages -ms	93.7	91.4	81.4	72.5	77.7	73.0	68.1	79.7	1.1
full testing set									
DeeperCut [15]	78.4	72.5	60.2	51.0	57.2	52.0	45.4	59.5	485
Iqbal et al. [16]	58.4	53.9	44.5	35.0	42.2	36.7	31.1	43.1	10
Ours-2 stages -ms	90.4	85.5	73.0	60.1	71.2	60.1	51.2	70.2	0.98
ours-6 stages	89.0	84.9	74.9	64.2	71.0	65.6	58.1	72.5	0.6
Ours-6 stages -ms	91.2	87.6	77.7	66.8	75.4	68.9	61.7	75.6	1.24

Table 1. Results on the MPII dataset. Top: Comparison result on the testing subset. Bottom: Comparison results on the whole testing set. Testing with three scale search is denoted as "-ms".

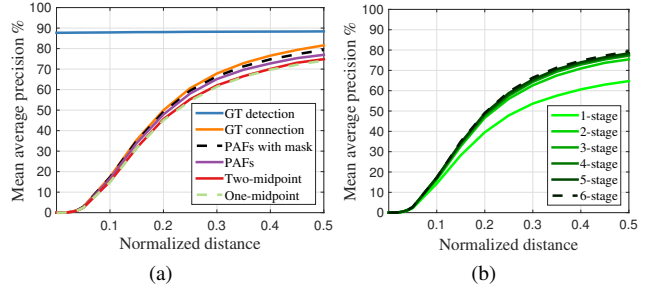


Figure 8. mAP curves over different PCKh threshold on MPII validation set. (a) mAP curves of self-comparison experiments. (b) mAP curves of PAFs across stages.

our method outperforms previous state-of-the-art bottom-up methods [15] with 8.5% AP higher. Remarkably, our runtime is two orders of magnitude less than theirs. In the second half of Table 1, we provide the results on the entire MPI testing set. Our method with 2 stages already outperforms previous state-of-the-art method by a large margin, i.e., 11% increase on AP. Using the model with 6 stages further increases the performance to 75.6% AP. The AP comparison with previous bottom-up approaches indicate the effectiveness of our novel feature representation, PAFs, to associate body parts. Using an optimization based on the tree structure, our method achieves better accuracy than a graphcut optimization formula based on fully connected graph structure as in [27, 15]. Note that our runtime reported is slower than our realtime system with normal video frames, because MPII testing set contains some large images after using the average people scale as defined in their evaluation method. We report a more detailed runtime analysis in Section 4.3.

Figure 8(a) shows the self-comparison results on our MPII validation set, i.e., 345 images excluded from training set. In the threshold of PCKh-0.5, the result using PAFs representation outperforms the results of using the midpoint representation, specifically, 2.9% higher than one-midpoint and 2.3% two-midpoint. The PAFs which encodes both position and orientation information of human limb is more robust to distinguish the common cross-over cases, e.g., overlapping arms. Training with masks of unlabeled persons further improves the performance by 2.3% because it avoids penalizing the true positive prediction in the loss dur-

ing training. If we use the ground-truth keypoint location with our parsing algorithm, we can obtain a AP of 88.3%. In Figure 8(a), the AP of our parsing with GT detection is constant across different PCKh thresholds due to no localization error. Using GT connection with our keypoint detection achieves a AP of 81.6%. It is notable that our parsing algorithm based on PAFs achieves a similar AP as using GT connections (79.4% vs 81.6%). This indicates parsing based on PAFs is quite robust in associating correct part detections. Figure 8(b) shows a comparison of performance across stages. The performance increases monotonically with the iterative refinement framework. Figure 7 shows the qualitative improvement of the predictions over stages.

4.2. Results on the MSCOCO Keypoints Challenge

The MSCOCO training set consists of over 100K person instances labeled with over 1 million total keypoints (i.e. body parts). The testing set contains “test-challenge”, “test-dev” and “test-standard” subsets, which have roughly 20K images each. The MSCOCO evaluation defines the object keypoint similarity (OKS) and uses the mean average precision (AP) over 10 OKS thresholds as main competition metric [1]. The OKS plays the same role as the IoU in object detection. It is calculated from scale of the person and the distance between predicted points and GT points. We submitted our results and our method won the first place in all test sets. Table 2 shows results from top teams in the challenge. We outperform other teams, which all use top-down methods. It is the noteworthy that our method has won, but has lower accuracy than the top-down methods on people of smaller scales (AP^M). The reason is that our method has to deal with a much larger scale range spanned by all people in the image in one shot. In contrast, top-down methods rescale the patch of each detected area to preferable size independently and thus suffer less from small people.

In Table 3, we report self-comparisons on a subset of the COCO validation set, i.e., 1061 images that are randomly selected. If we use the GT bounding box and a single person CPM [38], we can achieve a upper-bound for the top-down approach using CPMs, which is 62.7% AP. If we use the state-of-the-art object detector, Single Shot MultiBox Detector (SSD)[22], the performance drops 10%. This comparison indicates the performance of the top-down approach rely heavily on the person detector. In contrast, our bottom-up method achieves 58.4% AP. If we refine the results of our method by applying a single person CPM on each of the rescaled region of each estimated person parsed by our method, we gain an 2.6% overall AP increase. Note that we only update estimations on predictions that both method agree well enough, so the benefit purely come from better precision. We expect a larger scale search can further improve the performance of our bottom-up method. Figure 9 shows a breakdown of errors of our method on the

Team	AP	AP ⁵⁰	AP ⁷⁵	AP ^M	AP ^L
Test-challenge					
Ours	60.5	83.4	66.4	55.1	68.1
G-RMI	59.8	81.0	65.1	56.7	66.7
DL-61	53.3	75.1	48.5	55.5	54.8
R4D	49.7	74.3	54.5	45.6	55.6
Test-dev					
Ours	61.8	84.9	67.5	57.1	68.2
G-RMI	60.5	82.2	66.2	57.6	66.6
DL-61	54.4	75.3	50.9	58.3	54.3
R4D	51.4	75.0	55.9	47.4	56.7

Table 2. Results on COCO 2016 keypoint challenge. Top: results on test-challenge. Bottom: results on test-dev (top methods only). AP⁵⁰ is the AP at OKS=0.5, AP^L is the AP for large scale persons.

Method	AP	AP ⁵⁰	AP ⁷⁵	AP ^M	AP ^L
GT + CPM [15]	62.7	86.0	69.3	58.5	70.6
SSD[22]+CPM[15]	52.7	71.1	57.2	47.0	64.2
Ours - 6 stages	58.4	81.5	62.6	54.4	65.1
Ours + refinement	61.0	84.9	67.5	56.3	69.3

Table 3. Self-comparison experiments on COCO validation set.

MSCOCO validation set. Most of the false positives come from imprecise localization, other than background confusion. This indicates there is more room to improve in capturing spatial dependencies than in recognizing appearances.

4.3. Runtime Analysis

To analyze the runtime performance of our method, we collect videos with a varying number of people. The original frame size is 1080×1920 , which we resize to 368×654 during testing to fit in GPU memory. The runtime analysis is performed on a laptop with one NVIDIA GeForce GTX-1080 GPU. In Figure 9(d), we use person detection and single-person CPM as a top-down comparison, where the runtime is roughly proportional to the number of people in the image. In contrast, the runtime of our bottom-up approach increases very slowly with the increasing number of people. It contains two major parts: (1) CNN processing time whose runtime complexity is $O(1)$, constant with varying number of people. (2) Multi-person parsing time whose runtime complexity is $O(n^2)$, where n represents the number of people. However, the parsing time does not significantly influence the overall runtime because it is two orders of magnitude less than the CNN processing time, e.g., for 9 people, the parsing takes 0.58 ms while CNN takes 99.6 ms. Our method has achieved the speed of 8.8 fps for a video with 19 people.

5. Discussion

Moments of social significance, more than anything else, compel people to produce photographs and videos. Our photo-collections tend to capture moments we share with other people: birthdays, weddings, vacations, pilgrimages, sports events, graduations, family portraits, and so on. To

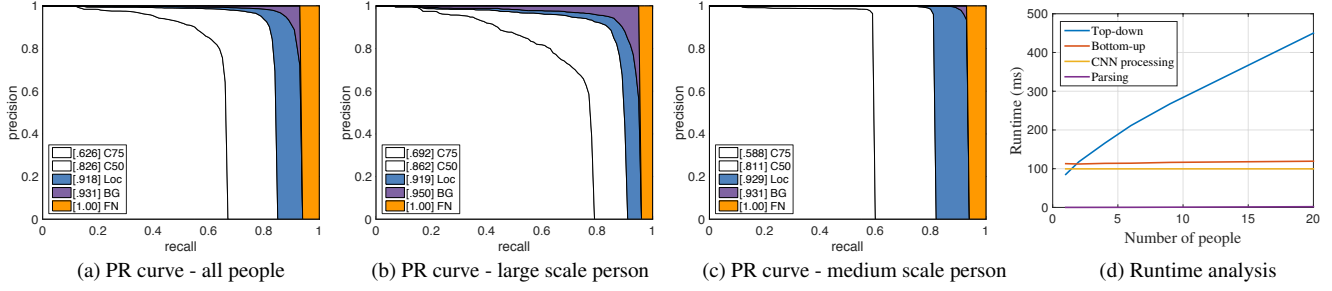


Figure 9. AP performance on COCO validation set in (a),(b) and (c) for Section 4.2, and runtime analysis in (d) for Section 4.3.

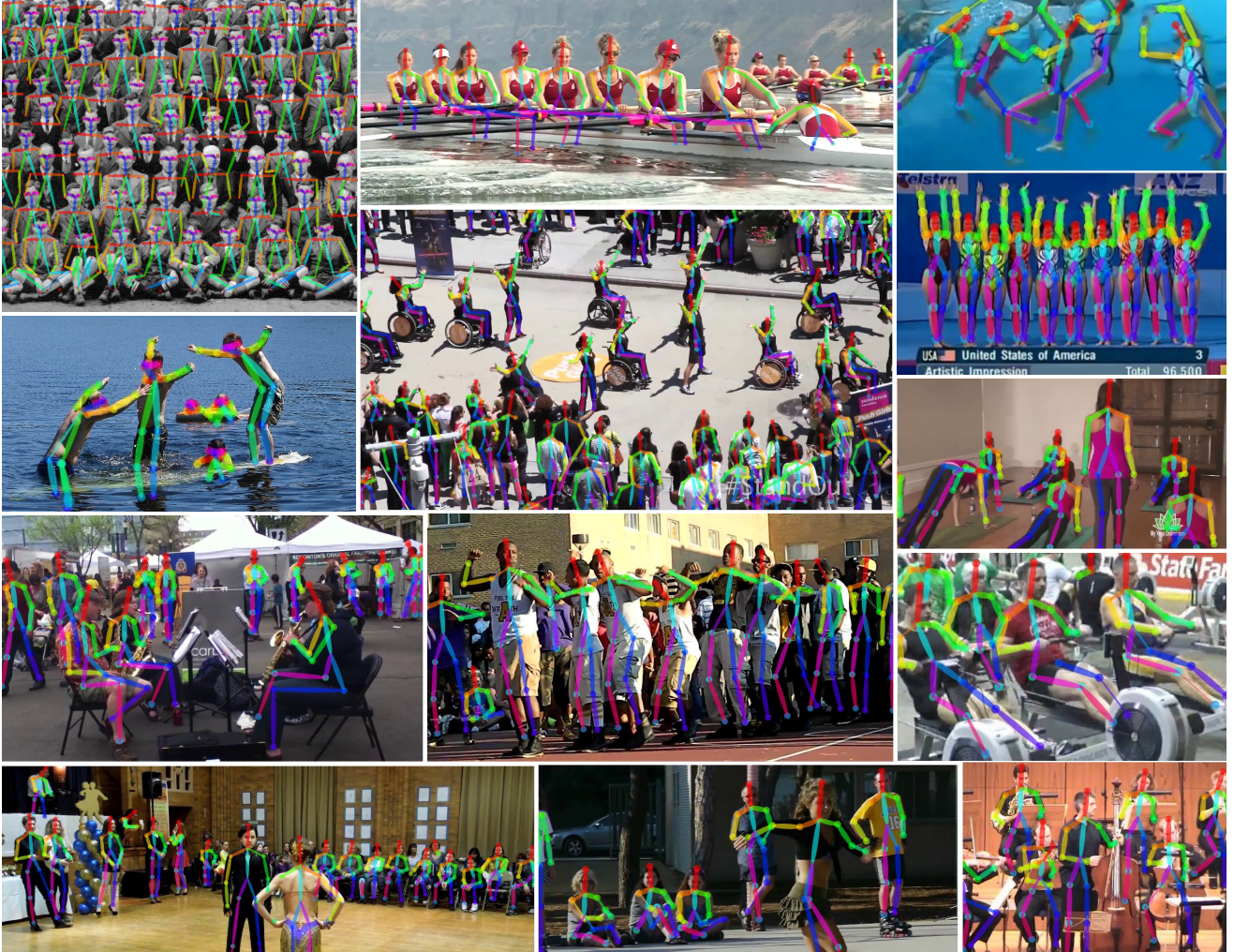


Figure 10. Results containing viewpoint and appearance variation, occlusion, crowding, contact, and other common imaging artifacts.

enable machines to interpret the significance of such photographs, they need to have an understanding of people in images. Machines, endowed with such perception in real-time, would be able to react to and even participate in the individual and social behavior of people.

In this paper, we consider a critical component of such perception: realtime algorithms to detect the 2D pose of multiple people in images. We present an explicit nonparametric representation of the keypoints association that en-

codes both position and orientation of human limbs. Second, we design a CNN architecture for jointly learning parts detection and parts association. Third, an efficient parsing algorithm is proposed to use the part affinity fields as important bridges to associate body part detection candidates and form the full body pose of all people in the image. We publicly release our code and models to ensure full reproducibility and to encourage future research in the area.

References

- [1] Mscoco keypoint evaluation metric. <http://mscoco.org/dataset/#keypoints-eval>. 7
- [2] M. Andriluka, L. Pishchulin, P. Gehler, and B. Schiele. 2d human pose estimation: New benchmark and state of the art analysis. In *CVPR*, 2014. 6
- [3] M. Andriluka, S. Roth, and B. Schiele. Pictorial Structures Revisited: People Detection and Articulated Pose Estimation. In *CVPR*, 2009. 2
- [4] M. Andriluka, S. Roth, and B. Schiele. Monocular 3D Pose Estimation and Tracking by Detection. In *CVPR*, 2010. 2
- [5] Y. Bengio, P. Simard, and P. Frasconi. Learning long-term dependencies with gradient descent is difficult. *IEEE Transactions on Neural Networks*, 1994. 2
- [6] A. Bulat and G. Tzimiropoulos. Human pose estimation via convolutional part heatmap regression. In *ECCV*, 2016. 1, 2
- [7] X. Chen and A. Yuille. Articulated pose estimation by a graphical model with image dependent pairwise relations. In *NIPS*, 2014. 2
- [8] M. Dantone, J. Gall, C. Leistner, and L. Van Gool. Human pose estimation using body parts dependent joint regressors. In *CVPR*, 2013. 2
- [9] M. Eichner and V. Ferrari. We are family: Joint pose estimation of multiple persons. In *ECCV*. Springer, 2010. 2
- [10] P. F. Felzenszwalb and D. P. Huttenlocher. Pictorial structures for object recognition. *IJCV*, 2005. 2
- [11] G. Gkioxari, B. Hariharan, R. Girshick, and J. Malik. Using k-poselets for detecting people and localizing their keypoints. In *CVPR*, 2014. 1, 2
- [12] X. Glorot and Y. Bengio. Understanding the difficulty of training deep feedforward neural networks. In *AISTATS*, 2010. 2
- [13] K. He, X. Zhang, S. Ren, and J. Sun. Deep residual learning for image recognition. *arXiv preprint arXiv:1512.03385*, 2015. 2
- [14] S. Hochreiter, Y. Bengio, P. Frasconi, and J. Schmidhuber. Gradient flow in recurrent nets: the difficulty of learning long-term dependencies, 2001. 2
- [15] E. Insafutdinov, L. Pishchulin, B. Andres, M. Andriluka, and B. Schiele. Deepcut: A deeper, stronger, and faster multi-person pose estimation model. *arXiv preprint arXiv:1605.03170*, 2016. 2, 3, 5, 6, 7
- [16] U. Iqbal and J. Gall. Multi-person pose estimation with local joint-to-person associations. *arXiv preprint arXiv:1608.08526*, 2016. 1, 2, 6
- [17] S. Johnson and M. Everingham. Clustered pose and non-linear appearance models for human pose estimation. In *BMVC*, 2010. 2
- [18] L. Karlinsky and S. Ullman. Using linking features in learning non-parametric part models. In *ECCV*, 2012. 2
- [19] H. W. Kuhn. The hungarian method for the assignment problem. *Naval research logistics quarterly*, 1955. 4
- [20] X. Lan and D. P. Huttenlocher. Beyond trees: Common-factor models for 2d human pose recovery. In *ICCV*, 2005. 2
- [21] T.-Y. Lin, M. Maire, S. Belongie, J. Hays, P. Perona, D. Ramanan, P. Dollár, and C. L. Zitnick. Microsoft coco: Common objects in context. In *ECCV*, 2014. 6
- [22] W. Liu, D. Anguelov, D. Erhan, C. Szegedy, and S. Reed. Ssd: Single shot multibox detector. *arXiv preprint arXiv:1512.02325*, 2015. 7
- [23] A. Newell, K. Yang, and J. Deng. Stacked hourglass networks for human pose estimation. *arXiv preprint arXiv:1603.06937*, 2016. 1, 2
- [24] W. Ouyang, X. Chu, and X. Wang. Multi-source deep learning for human pose estimation. In *CVPR*, 2014. 2
- [25] T. Pfister, J. Charles, and A. Zisserman. Flowing convnets for human pose estimation in videos. In *ICCV*, 2015. 2
- [26] L. Pishchulin, M. Andriluka, P. Gehler, and B. Schiele. Poselet conditioned pictorial structures. In *CVPR*, 2013. 2
- [27] L. Pishchulin, E. Insafutdinov, S. Tang, B. Andres, M. Andriluka, P. Gehler, and B. Schiele. Deepcut: Joint subset partition and labeling for multi person pose estimation. *CVPR*, 2016. 2, 3, 5, 6
- [28] L. Pishchulin, A. Jain, M. Andriluka, T. Thormählen, and B. Schiele. Articulated people detection and pose estimation: Reshaping the future. In *CVPR*, 2012. 1, 2
- [29] V. Ramakrishna, D. Munoz, M. Hebert, J. A. Bagnell, and Y. Sheikh. Pose machines: Articulated pose estimation via inference machines. In *ECCV*, 2014. 2
- [30] D. Ramanan, D. A. Forsyth, and A. Zisserman. Strike a Pose: Tracking people by finding stylized poses. In *CVPR*, 2005. 2
- [31] L. Sigal and M. J. Black. Measure locally, reason globally: Occlusion-sensitive articulated pose estimation. In *CVPR*, 2006. 2
- [32] K. Simonyan and A. Zisserman. Very deep convolutional networks for large-scale image recognition. *arXiv preprint arXiv:1409.1556*, 2014. 5
- [33] M. Sun and S. Savarese. Articulated part-based model for joint object detection and pose estimation. In *ICCV*, 2011. 1, 2
- [34] J. Tompson, R. Goroshin, A. Jain, Y. LeCun, and C. Bregler. Efficient object localization using convolutional networks. *arXiv preprint arXiv:1411.4280*, 2014. 2
- [35] J. J. Tompson, A. Jain, Y. LeCun, and C. Bregler. Joint training of a convolutional network and a graphical model for human pose estimation. In *NIPS*, 2014. 2
- [36] A. Toshev and C. Szegedy. Deeppose: Human pose estimation via deep neural networks. In *CVPR*, 2014. 2
- [37] Y. Wang and G. Mori. Multiple tree models for occlusion and spatial constraints in human pose estimation. In *ECCV*, 2008. 2
- [38] S.-E. Wei, V. Ramakrishna, T. Kanade, and Y. Sheikh. Convolutional pose machines. *CVPR*, 2016. 1, 2, 3, 5, 6, 7
- [39] D. B. West et al. *Introduction to graph theory*, volume 2. Prentice hall Upper Saddle River, 2001. 4
- [40] Y. Yang and D. Ramanan. Articulated pose estimation with flexible mixtures-of-parts. In *CVPR*, 2011. 2
- [41] Y. Yang and D. Ramanan. Articulated human detection with flexible mixtures of parts. *TPAMI*, 2013. 3